Accepted manuscript doi:
10.1680/jgeot.23.00162

Accepted manuscript doi:
10.1680/jgeot.23.00162

Submitted: 27 May 2023

Published online in 'accepted manuscript' format: 29 March 2024

Manuscript title: Exploring the micro-to-macro response of granular soils with real particle shapes via μCT-aided DEM analyses

Authors: Yang Li*,†, Masahide Otsubo*,‡, Vasileios Angelidakis[§,‖], Reiko Kuwano* and Sadegh Nadimi[§]

Affiliations: *Institute of Industrial Science, The University of Tokyo, Meguro-ku, Tokyo, Japan; †McCormick School of Engineering, Northwestern University, Evanston, IL, USA; ‡Public Works Research Institute, Tsukuba, Ibaraki, Japan; §School of Engineering, Newcastle University, Newcastle upon Tyne, UK and ‖School of Natural and Built Environment, Queen's University Belfast, Belfast, UK

Corresponding author: Masahide Otsubo, Institute of Industrial Science, The University of Tokyo, 4-6-1 Komaba, Meguro-ku, Tokyo, 153-8505, Japan.

E-mail: ootsubo-m573cm@pwri.go.jp

Accepted manuscript doi:
10.1680/jgeot.23.00162

Abstract

This contribution provides high fidelity images of real granular materials with the aid of X-ray micro computed tomography (μCT), and employs a multi-sphere representation to reconstruct non-spherical particles. Through the discrete element method (DEM) simulations on granular samples composed of these non-spherical clumps, the effect of particle shape on the macroscopic mechanical response and microscopic soil fabric evolution is examined for soil assemblies under triaxial compression. Simulation results indicate that materials with more irregular particles tend to show higher shear resistance in both peak and critical states, while exhibiting higher void ratio under isotropic loading conditions and in the critical state. The proposed critical state parameters for describing the sensitivity of the mean coordination number to confining pressures are larger as particles become more irregular. At a microscopic level of observation, directional and scalar parameters of particle contacts are sensitive to predefined particle asperities. More irregular materials appear to exhibit higher fabric anisotropy regarding particle orientation in the critical state, while branch vector is affected by both contact modes and particle shape. The critical stress ratio from the simulation results is validated by comparing with experimental results, and further found to be linearly linked to the shape-weighted fabric anisotropy indices.

Keywords: Shear strength; Particle scale behaviour; Fabric of soils; Anisotropy; Discrete-element modelling

Accepted manuscript doi:
10.1680/jgeot.23.00162

1. Introduction

For granular materials the term 'particle shape' informs the overall form, local angularity and surface texture of a particle at three different aspects of observation (Barrett, 1980). Particle shape can be quantitatively described by shape parameters. Krumbein and Sloss (1963) provided an intuitive shape chart based on sphericity (S) and roundness (R). Altuhafi *et al*. (2013) applied dynamic image analysis (DIA) to enable the calculation of sphericity (S), convexity (C_x) and aspect ratio (AR). Researchers have continued to develop new shape parameters to better capture the role of particle shape in geomechanics, including overall regularity (OR) (Yang and Luo, 2015) and shape angular group indicator ($SAGI$) (Altuhafi *et al*., 2016). Angelidakis *et al*. (2022) proposed new interpretation of elongation (El), flatness (Fl) and compactness (Co) to better describe the particle form in a three-dimensional perspective. In this contribution, sphericity (S), convexity (C_x), aspect ratio (AR) and overall regularity (OR) are employed and their definitions are given in the Appendix where greater values of these particle shape parameters indicate a *more sphere-like/less irregular* shape; whereas lower values indicate the opposite.

At a small strain range (typically $\leq 10^{-5}$), small strain shear stiffness (G_0) can be expressed as a function of mean effective stress (p') and void ratio (e) as:

$$G_0 = aF(e)\left(\frac{p'}{101.3\text{kPa}}\right)^b \tag{1}$$

where a and b are material-dependent constants that determine G_0, and $F(e)$ represents the void ratio correction function proposed by Hardin and Richart (1963). For an extensive deformation where the intermediate principal stress equals to the minor principal stress under dry and drained triaxial compression, granular materials exhibit a unique critical state characterised by two equations:

$$q = Mp' \tag{2}$$

$$e = e^{\Gamma} - \lambda \ln p' \tag{3}$$

where q is the deviator stress $q = \sigma_1^{'} - \sigma_3^{'}$, in which $\sigma_1^{'}$ and $\sigma_3^{'}$ are major and minor principal stresses, respectively; M , e^{Γ} , λ are critical state parameters.

The significance of particle shape in the abovementioned soil characteristics from the small-strain regime to the critical state is widely recognised by experimentalists. Cho *et al*. (2006) and Altuhafi *et al*. (2016) revealed that more irregular particles can attain higher maximum (e_{max}) and minimum void ratios (e_{min}). Cho *et al*. (2006) reported that increasing particle irregularity reduces the small strain stiffness (lower a) while increasing stress sensitivity (greater b). However, Altuhafi *et al*. (2016) found that G_0 normalised by the coefficient of uniformity (C_u) tends to increase with irregularity. The latter observation was supported by experiments on granular mixtures composed of different fractions of particle shapes (Shin and Santamarina, 2013; Liu and Yang, 2018). Additionally, Chang *et al*. (1991) proposed a value of b =1/3 for Hertzian contacts between spheres; while experimental results gave a range of b being 0.32 to 0.72 (Cho *et al.*, 2006; Altuhafi *et al*., 2016). A consensus on the effect of particle shape on G_0 has not been achieved because of these contradictory findings.

Concerning critical state parameters, Cho *et al*. (2006) reported that increasing particle irregularity leads to decreases in e^{Γ} and λ ; however, Altuhafi *et al*. (2016) found the same trend for e^{Γ} whereas a less obvious relation between λ and particle shape. Yang and Luo (2015) mixed Fujian sands and glass beads and found decreasing trends of M and λ as particles become more irregular. Xiao *et al*. (2019) mixed two different shaped glass beads and found increases in critical stresses for more irregular particles. Wu *et al*. (2021) tested Clinker ash in drained triaxial tests and observed decreasing trends of e^{Γ} and λ as particles become less irregular. Overall, the sensitivity of M , e^{Γ} , λ to particle shape has become clearer with the advancement of experimental technology.

Accepted manuscript doi:
10.1680/jgeot.23.00162

On the other hand, discrete-element method (DEM) studies that use disks or spheres lack natural particle rolling resistance and particle interlocking, which crucially affect the mechanical characteristics of real granular materials (Zhao *et al.*, 2023). To better represent realistic soil behaviour, non-spherical particles such as super-ellipsoids (*e.g.* Zhao *et al*., 2017), sphere-clusters (*e.g.* Nguyen *et al*., 2021), sphere-clumps (Katagiri *et al.*, 2010), level-set functions (Kawamoto *et al*., 2016, 2018) and spherical harmonics (*e.g.* Xu *et al*., 2021) have been used in DEM simulations. Zhao *et al*. (2017) found that the densest packing density appears at AR =0.3, while not spheres (AR =1). Nguyen *et al*. (2021) examined the sensitivity of critical state parameters to particle shape and found decreasing trends of M and λ with S, in line with Yang and Luo (2015); while an increasing trend of e^{Γ} with S, different from that in Cho *et al*. (2006). Xu *et al*. (2021) observed an increase in shear strength in both peak and critical states with increasing particle irregularity. They also found that more irregular materials tend to develop more significant stress-induced fabric anisotropy during the loading process.

X-ray micro computed tomography (μCT) enables the acquisition of detailed images of granular materials, allowing for the replication of complex shapes in simulation. Zhang *et al*. (2021) generated non-spherical particles based on Ottawa sands and found that particles having more irregular materials achieve looser packing conditions (*i.e.* higher e) during isotropic compression. Nie *et al*. (2021) simulated Leighton Buzzard sand (LBS) and reported that the mean coordination number ($\bar{Z}$) reduces while the mean contact force grows with the decrease of OR. Otsubo *et al.* (2023) used a μCT image of an LBS particle to systematically investigate the influence of grain shape and surface asperity on G_0. They revealed that particle morphology imposes a difference in total contact area between particles, leading to a variation of G_0. However, these DEM studies did not consider a wide variability of particle shapes typically observed in geotechnical experimentation. To this end, practical protocol of simulation campaigns needs to be established to investigate the universality of particle shape effects on the mechanical behaviour of granular materials.

This contribution applies μCT to acquire three-dimensional images from a wide selection of real granular materials. Non-spherical clumps are generated to provide multi-sphere representations for these real particles. DEM simulations of drained triaxial compressions are conducted from small to large strains using the generated clumps, to investigate how particle shape affects the macroscopic mechanical response and microscopic soil fabric evolution throughout the triaxial loading. Finally,

this contribution aims to establish a micro-to-macro connection between critical deviator stress ratio and internal fabric anisotropy, linking experimental and simulation observations which incorporate particle shape.

2. Particle generation from μCT imaging data

Spherical, deformed, clumped and angular glass beads (SGB, DGB, CGB and AGB), silica sand (SS) and Leighton Buzzard sand (LBS) were scanned, where the abbreviated names were used to label and distinguish different materials in the laboratory experimentation as outlined in Li *et al*. (2024). The resolution of the images was 17.62 μ m for glass beads, 11.65 μ m for SS and LBS in voxel sizes, respectively. This means that a sand grain with a diameter of 1 mm is represented by approximately 86 voxels across its diameter. Due to the high shape variability of CGB and AGB, two grains were selected for each, noted as CGB1, CGB2 and AGB1, AGB2, respectively. Therefore, eight different shapes were selected to investigate the effects of particle shape on micro-to-macro responses in this contribution.

Clump generation

Fig. 1 shows the main image processing operations for a slice of the silica sand particle. The three-dimensional μCT image was first binarised by identifying the solid phase of each material using the thresholding technique in Otsu (1979). To separate neighbouring touching particles, the watershed segmentation algorithm was adopted in three-dimensions as detailed in Nadimi and Fonseca (2018). After segmentation, each particle was marked with a unique label with individual particle geometry information. The labelled μCT images of the materials of interest were analysed to identify all the different particles and approximate their morphology using multi-sphere representations, *i.e.* sets of rigidly connected overlapping sub-spheres. The use of this method feasibly preserved the concavity of non-spherical particles to capture the particle interlocking. This operation was performed using the open-source software: Code Library to generate Universal Multi-sphere Particles (CLUMP) (Angelidakis *et al.*, 2021a). The multi-sphere clumps were generated based on the Euclidean Distance Transform of three-dimensional images. Each sub-sphere was generated at a location where the mass of the particle was most represented in each iteration of the procedure. According to strategy, the first sub-sphere was always the largest possible inscribed sphere, while each subsequent one was smaller than its previous iteration. With this method, particles can be generated at predefined fidelity levels with a given overlap ratio between sub-spheres, which was

adjusted as 0.2 to 0.45 in this contribution. This overlap ratio determined the ratio between the overlap distance and the radius of the later generated sub-sphere between two connected sub-spheres in every iteration based on the Euclidean distance transform.

Shape characterisation

A surface extraction algorithm within the CLUMP software allows for the tessellation of the surface of the generated multi-sphere particles, which can be used to quantify their shape parameters. Utilising the labelled particle images of the analysed materials, shape characteristics of the generated clumps and original particles from the μCT were calculated using the open-source software: SHAPE Analyser for Particle Engineering (SHAPE) (Angelidakis *et al.*, 2021b). Here, the minimal-volume Oriented Bounding Box of each particle was used to calculate its main particle dimensions. It becomes evident in literature that the same shape parameter may be defined in many different ways. To this end, the formulae used to calculate S, C_x, AR and OR in this contribution are listed in Appendix.

Determination of sufficient number of sub-spheres to represent real particle shapes using clumps

To achieve an optimal balance between simulation efficiency and morphological fidelity of the non-spherical particles in DEM simulations, the number of sub-spheres per particle (N_s) needs to be decided so as to minimise the difference in shape parameters between the clump and real particles.

Fig. 2 demonstrates the variation of S, C_x, AR and OR for generated clumps with N_s=1, 2, 3, 5, 10, 25, 100, 200, 500 using an SS particle example, where the images of clumps are provided to visualise how particle morphology evolves with N_s. The generated clump fills more volume enclosed by the surface mesh of the original SS particle with the increase of N_s. All shape parameters drop markedly with the increase of N_s; especially, S, C_x and OR decrease until N_s=25, followed by a plateau for larger N_s; AR noticeably reduces from N_s=1 to N_s=2 and slightly increases with increasing N_s. After similar comparisons, the other considered shapes present stable values of shape

parameters no later than N_s =25, where only a small relative variation can be observed. Table 1 lists the shape parameters of the reconstructed clumps with N_s =25, along with those for μCT images of the corresponding real particles. All parameters of clumps, except AR, have similar values to those of μCT images within a relative difference smaller than 7%, revealing a reliable representation of original particle morphology. It appears that more satellite sub-spheres may be needed for CGB2 and AGB2 to accurately reconstruct clump dimensions closer to the real particle in the three principal directions, which leads to closer AR values to real particles.

Additionally, Otsubo *et al*. (2023) applied the same algorithm to generate clump LBS particles and found that the stress responses become similar for simulations throughout the entire triaxial loading with $N_s \geq 10$. Katagiri (2019) conducted a series of isotropic compression tests using clumps to simulate Toyoura sand and found that void ratio and mean coordination number in the isotropic state do not change significantly beyond a threshold of N_s =14. According to the parametric study and relevant literature, N_s =25 was decided as a sufficient number of sub-spheres for a safe side to generate representative non-spherical clumps for subsequent simulations, specifically for the particle shapes considered in this contribution.

Fig. 3 presents non-spherical clumps of the studied materials with N_s =25 sub-spheres, except for SGB which were represented by a single sphere. The clump generation technique of Favier *et al.* (1999) was used to create the clumps for DGB since its axisymmetric shape. Referring to Table 1, SGB takes a value of 1.0 for all shape parameters, while CGB2 shows the lowest C_x value because of its special cluster formation; AGB1 and AGB2 have the lowest AR due to their planar shapes.

Accepted manuscript doi:
10.1680/jgeot.23.00162

3. DEM simulation method

Material properties

This contribution adopted a modified version of LAMMPS (Plimpton, 1995; Nguyen and Plimpton, 2019), which allowed for a robust implementation of the simplified Hertz-Mindlin (HM) contact model (Itasca Consulting Group, 2007). In comparison to the linear contact model, HM contact model can capture more realistic non-linear contact behaviours (Johnson, 1985). The simplified HM contact law was applied to each sub-sphere in non-spherical clumps, this scheme enables that the local asperities of the non-spherical clumps can be reflected in the contact behaviours. Specifically, the smaller sub-spheres in contact exhibit a softer contact stiffness with a given contact force. Therefore, the use of clumps facilitated a more systematic investigation on how the mechanical response evolves from a sphere to a non-spherical clump. The material properties were a material density of ρ_p =2500 kg/m^3, Young's modulus of E_p =64.5 GPa and Poisson's ratio of v_p =0.23.

Following O'Sullivan and Bray (2004), a density scaling factor of 1000 was applied to enhance computational efficiency. The material properties were uniformly assigned to each sub-sphere, where the mass and moments of inertia of overlapped regions were excluded. A linear particle size distribution (PSD) was identically assigned to every material as 0.6-1.2 mm. The minimum volumetric ellipsoid (MVE) method was applied to generate packings made of non-spherical clumps (Zheng and Hyrciw, 2017), where circumscribed spheres were generated using the given PSD, which were then replaced by the non-spherical clumps used in each simulation scenario.

Simulation procedure

Periodic boundaries were employed in the three principal directions of the simulated samples. Using periodic boundary conditions, when a particle crosses one boundary of the simulation domain, it reappears on the opposite boundary with the same velocity and material properties. These boundary conditions offer the advantage of avoiding initial heterogeneity in soil fabric such that the number of particles for a sample can be efficiently optimised (Thornton, 2000). The sample was composed of 5000 spheres for SGB and 5000 non-spherical clumps (1.25×10^5 nominal sub-spheres). All clumps were generated in a cubic space without initial particle contacts in the absence of gravity. Subsequently, the cloud of particles was compressed under an isotropic stress of 50 kPa using a servo-control scheme, which ensures a stable equilibrium for the generated non-spherical clumps following

Morimoto *et al.* (2021). All granular samples were compressed with the interparticle friction coefficient of μ_{iso}=0.001 which ensured the densest condition in the DEM environment, serving as an analogy of relative density = 100% for a given shape. A representative cubic sample is given in Fig. 4, which consists of the non-spherical clump made of N_s=25 using the imaging data of an SS particle.

After undergoing isotropic compression, all samples were loaded in the vertical direction (1-axis in Fig. 4) under dry and drained conditions, considering an interparticle friction coefficient of μ_{shear} =0.35. The triaxial loading was performed at a constant strain rate of 0.002 [s^{-1}], while maintaining the minor principal stress as $\sigma_2^{'} = \sigma_3^{'}$=50 kPa. This loading rate was employed to ensure quasi-static loading conditions as in Lopera Perez *et al.* (2016). Local damping (ζ_{local}) and viscous damping (ζ_{vis}) were omitted in the isotropic compression; on the other hand, ζ_{local}=0.1 and ζ_{vis}=0.05 were applied during triaxial compression to suppress kinetic energy and minimise dynamic effects. Besides, ζ_{local} and ζ_{vis} were deactivated during small-strain probing tests to evaluate G_0. According to Otsubo *et al.* (2017), a timestep (Δt) of 2×10^{-6} s was selected for simulations with SGB, and the same was used for non-spherical clumps.

4. Macroscopic mechanical responses

Overall stress/strain and packing characteristics

Fig. 5 compares the deviator stress (q) and volumetric strain (ε_v) for all tested materials with axial strain (ε_a) under the densest possible condition, where the images of non-spherical clumps are annotated for reference. Overall, granular samples demonstrate significantly different responses due to different particle shapes. SGB shows the lowest stress level and minimal dilation. On the other hand, DGB initially experiences a noticeable increase in q, reaching its peak value the earliest among all particles, while displaying the second lowest stress level in the critical state. AGB1 and AGB2 show

less significance of strain softening, even under the densest conditions. ε_v for AGB2 gradually develops to show the latest onset of phase transformation point, but demonstrates the second most significant dilation at ε_a =40%. CGB2 gives the highest stress levels, particularly in the peak state and the most marked dilation upon shearing, while LBS and SS show intermediate stress levels and volumetric change among these materials. It is noted that the initially dramatic increase in q (shown in the inset) that is different from conventional laboratory experiments is attributed to the manual adjustment of μ_{shear}, as explained by Li *et al*. (2021).

Fig. 6 explores the changes in void ratio (e) and mean coordination number ($\bar{Z}$) with ε_a. e continuously increases while $\bar{Z}$ dramatically drops initially and stabilises with straining. This initially substantial reduction in $\bar{Z}$ results from the rapid collapse in horizontal contacts in the granular assembly while the subsequent stable $\bar{Z}$ value mainly reflects the particle contacts in the loading direction to form stress chains, as elucidated by Li *et al*. (2022a). CGB2 and AGB2 exhibit much higher e values throughout the loading; however, they show the greatest stress levels in the peak and critical states. This highlights the more dominant role the particle shape than initial density in the stress response while both are interplaying. DGB and CGB1 attain a lower e value than SGB in the isotropic state but end up with a similar e with SGB in the critical state. SGB and DGB display a markedly lower $\bar{Z}$ than other particles at later stable stages after the initial reduction. For irregular particles, CGB2, AGB1 and AGB2 show a higher $\bar{Z}$ compared with LBS and SS.

Relations between mechanical responses and shape parameters

Fig. 7a reveals the relations between peak/critical deviator stress ratios ($(q/p')_{peak}$, $(q/p')_{cri}$) and shape parameters (S, C_x, AR and OR). $(q/p')_{peak}$ and $(q/p')_{cri}$ increase as the employed shape parameters reduce, indicating that more irregular particles have higher shear resistance in the peak and critical states. Indicated by the semi-transparent shading, $(q/p')_{cri}$ can be better correlated than $(q/p')_{peak}$ with shape parameters; specifically, AGB gives a lower $(q/p')_{peak}$ than CGB2

despite having similar OR. This indicates that peak stress is more related to the particle interlocking or sliding/rolling motions. It is noted that $\varepsilon_{v,cri}$ with shape parameters is not provided as its trend is similar to that of void ratio with shape parameters under dry and drained conditions.

Fig. 7b compares the relations between isotropic/critical void ratios (e_{iso} and e_{cri}) and shape parameters. Samples containing more sphere-like particles can achieve denser packings in the isotropic and critical states. e_{iso} here can be considered as an analogy of densest attainable void ratio (e_{min}) in the laboratory. This decreasing trend is consistent with experimental results in Altuhafi *et al*. (2016). As shown in Fig. 7b and Table 2, e_{iso} values for DGB and CGB1 are lower than that of SGB, e_{cri} for DGB is also lower than that of SGB. Compared with SGB, DGB and CGB1 have similar S and C_x, but a lower AR. This is in agreement with Salot *et al*. (2009), who reported that slightly elongated particles can achieve denser packings than idealised spheres.

Fig. 7c explores the changes in mean coordination numbers in the isotropic and critical states ($\overline{Z_{iso}}$ and $\overline{Z_{cri}}$) with shape parameters. A two-phase variation of $\overline{Z_{iso}}$ with shape parameters can be observed: CGB2, LBS and AGB1, 2 demonstrate $\overline{Z_{iso}}$ being around 12 despite variations in their shape parameters, whereas others show a decreasing trend in $\overline{Z_{iso}}$ for more sphere-like materials. This is because asperity-to-asperity contacts were quantified rather than clump-to-clump contacts *i.e.* identifying contacts between sphere-elements of a clump instead of those between non-spherical clumps; Otsubo *et al*., (2023) reported that $\overline{Z_{iso}}$ of LBS particles is around 12 for asperity-to-asperity contacts while it is around 8 for clump-to-clump contacts at their densest packing configuration.

Small strain properties and critical state parameters

Small strain shear stiffness (G_0) was estimated under isotropic stresses of 50, 100, 200 and 400 kPa using static probing, *i.e.* linear stress-strain relation at a strain range of 10^{-5} (Kuwano and Jardine, 2002). According to Hardin and Richart (1963), the void ratio correction function in Eq. 1 was interpreted as $F(e)=(B-e)^2/(1+e)$. Following Iwasaki and Tatsuoka (1977), Kuwano and Jardine (2002) and Liu and Yang (2018), this contribution used B =2.17 for all tested materials.

According to Fig. 8, a in Eq. 1 decreases with the increase of shape parameters, which is contradictory to the experimental observations summarised in Cho *et al.*, (2006). Liu and Yang (2018) used materials with identical uniformity coefficients (C_u) and argued that the effect of C_u on G_0 should not be neglected, as also pointed out by Wichtmann and Triantafyllidis (2009) and Li *et al*. (2022b). The present contribution used identical C_u for all materials so that the reduction in a is consistent with that in Liu and Yang (2018). However, b values (Eq. 1) are found insensitive to shape parameters with b ≈0.35 (Table 2) for all materials. This value is close to the theoretical value of 1/3 based on the Hertzian contact law and effective medium theory (Chang *et al*., 1991), irrespective of particle shape. Otsubo *et al*. (2023) found that b is sensitive to N_s, implying that surface topography is governing the stress-sensitivity of G_0, which was effectively supported by Otsubo and O'Sullivan (2018). This contribution used a consistent N_s =25 for non-spherical clumps, suggesting that varying N_s is needed to capture b of experimental data.

The critical state parameters can be estimated according to Eqs. 2 and 3 using the samples mentioned above, which were sheared to the critical state (ε_a =40% in this contribution). The critical state parameters are plotted against shape parameters in Figs. 9 and 10 along with reference data from literature (Xie *et al.*, 2017; Jiang *et al.*, 2018; Nguyen *et al*., 2021; Nie *et al.*, 2021). In Figs. 9 and 10, the equations of the linear trendlines are provided with the determination of coefficient of determination (R^2) for the use of indicating the evolving trends with reliability. M decreases with

the increase of shape parameters, in agreement to Nie *et al*. (2021) and Nguyen *et al*. (2021). Yang and Luo (2015) experimentally reported a qualitatively decreasing trend for *M* using Fujian sands. λ and e^{Γ} also show decreasing trends as particles become less irregular. This trend aligns with the results observed in Nie *et al.* (2021) while Nguyen *et al*. (2021) displayed a contradictory trend in their DEM simulations. In contrast, e^{Γ} gives a good comparison between this contribution and past studies. In terms of R^2, it appears that C_x gives the lowest value, which indicates that the convexity conditions of the particles may not dominantly govern the mechanical responses in the critical state, whereas contributing to the particle interlocking more evidently reflected in the peak stress strength.

According to Fig. 6, $\bar{Z}$ approaches an identical value for each particle shape in the critical state. Similarly, Eq. 4 is proposed to capture a unique relation between $\bar{Z}$ and p':

$$\bar{Z} = \bar{Z}^{\Gamma} + \lambda_{\bar{Z}} \ln p' \tag{4}$$

where $\bar{Z}^{\Gamma}$ and $\lambda_{\bar{Z}}$ are the intercept and slope in the $\bar{Z}$ - p' relation with varying confining stresses in the critical state. Fig. 11 portrays the variations of $\bar{Z}^{\Gamma}$ and $\lambda_{\bar{Z}}$ with shape parameters. A lower $\bar{Z}^{\Gamma}$ is achieved for more sphere-like materials for a given stress level in the critical state. $\lambda_{\bar{Z}}$ decreases with the increase of particle shapes, indicating that more irregular materials have a higher sensitivity of $\bar{Z}$ to stress level in the critical state.

5. Microscopic fabric evolution

Evolution of soil fabric indices

The microstructure network of granular samples is described by various directional fabric indices, including contact normal (CN), particle orientation (PO) and branch vector (BV). CN refers to the vector normal to the contact plane for asperity-to-asperity contacts; PO describes the non-spherical particle's major axis orientation; BV is defined as the vector connecting the centroids of two contacting particles.

Following Fonseca *et al.*, (2013), ψ is defined as the inclination between the unit vectors of the abovementioned soil fabric indices and the horizontal plane (2-3 plane), as depicted in the insets in Fig. 12; further, ψ^{CN}, ψ^{PO} and ψ^{BV} are the angles regarding CN, PO and BV, respectively. Fig. 12 shows the normalised frequency distribution of ψ^{CN}, ψ^{PO} and ψ^{BV} at selected ε_a throughout loading for SS. In this context, the vertical axis refers to the normalised frequency, indicating the ratio between the number of vectors within an examined angle range and the total number of vectors. The theoretical normalised frequency distribution is derived from an enumeration of the unit vectors that describe all the orientations originating from the centre of a unit sphere. By comparison, the distributions in the isotropic state closely align with the theoretical distribution, confirming the homogeneity of samples in terms of soil fabric. Once upon loading, particle contacts are progressively dominant in a ψ^{CN} value between 30° to 40°. Similarly, ψ^{BV} distributions gradually show the peak between 15° to 25° with loading. Differently, ψ^{PO} shows a rather monotonic distribution with fewer and fewer particles orientated with a larger ψ^{PO}. Throughout loading, an increasing number of particles align their major axes with ψ^{PO} <30°.

A second-order tensor is utilised to quantify soil fabric (Oda, 1982):

$$\Phi_{ij} = \frac{1}{N}\sum_{k=1}^{N} n_i^k n_j^k \tag{5}$$

where N is the total number of vectors existing in the granular system, n_i^k and n_j^k are the unit orientation vectors alongside i and j directions, respectively. Referring to Fig. 4, Φ_{11} represents the component of soil fabric tensor in the loading direction while $(\Phi_{22} + \Phi_{33})/2$ stands for that perpendicular to the loading direction where $\Phi_{22} \approx \Phi_{33}$ was confirmed.

Fig. 13 visualises the three-dimensional distributions of the three normalised soil fabric indices for SS at sequential loading stages, following the interpretation by Zhao and Zhou (2017). At ε_a=0%, CN, PO and BV display approximately symmetric polar distributions, signifying the fabric isotropy prior to the initiation of triaxial compression. Subsequently, CN becomes more pronounced in the vertical direction, and its orientation remains relatively stable in the later stages of loading. In contrast, PO exhibits a more noticeable distributions in the horizontal plane. Interestingly, BV initially evolves to be more vertically orientated, but this anisotropic tendency diminishes as the as the distribution turns to be less significant after ε_a=13.0%.

To quantify the evolution of soil fabric indices, the fabric ratio is calculated as $\Phi = \Phi_{11} / \left[\left(\Phi_{22} + \Phi_{33} \right) / 2 \right]$ to represent the fabric anisotropy of the granular samples during shearing. Φ^{CN}, Φ^{PO} and Φ^{BV} are defined as fabric anisotropy indices for CN, PO and BV, respectively. Fig. 14 illustrates the variations of Φ^{CN}, Φ^{PO} and Φ^{BV} against ε_a upon loading using the examples of SS and CGB2. Φ^{CN} increases and subsequently tends to be stable for both SS and CGB2. In contrast, Φ^{PO} continuously decreases upon loading and tends to be stable in the critical state, giving value consistently lower than 1. As non-spherical clumps were randomly created with an isotropic Φ^{PO} (*i.e.* Φ^{PO}=1), this discloses that non-spherical particles undergo particle rearrangement during shearing and tend to align their major axes perpendicular to the loading direction. Interestingly, Φ^{BV} of SS and CGB2 shows different variations; Φ^{BV} of SS gradually increases and then gently decreases, supporting the visualisation in Fig. 13; whereas that of CGB2 initially increases but reduces markedly with further shearing and appears to evolve below the fabric isotropic line, which indicates that BV of CGB2 is first vertically significant but subsequently horizontally significant with shearing. This can be attributed to the fact that BV is not only influenced by contact condition but also by particle shape. More irregular materials with a low AR may exhibit horizontally significant fabric anisotropy concerning BV as loading continuously induces particle rearrangement.

The deviator part of the fabric tensor can be defined as:

$$c_{ij} = \frac{15}{2} \Phi_{ij}^{'}, \text{ where } \Phi_{ij}^{'} = \Phi_{ij} - \frac{1}{3} \Phi_{ii} \quad (6)$$

A scalar parameter can be then introduced according to the invariant of $\Phi_{ij}^{'}$ as follows:

$$a_c = \sqrt{\frac{3}{2} c_{ij} \cdot c_{ij}} \tag{7}$$

Furthermore, a_c^{CN}, a_c^{PO} and a_c^{BV} are defined as anisotropy degrees for CN, PO and BV, respectively.

Fig. 15 provides the variations of a_c for CGB2 and SS in terms of CN, PO and BV during loading. In comparison to Fig. 14, the variations of a_c^{CN} are similar, gradually increasing and eventually stabilising. The variations of a_c^{PO} increase progressively prior to a relatively mild trend. Especially, a_c^{BV} for SS first increases and then decreases as similar to the variation of Φ^{BV}; however, a_c^{BV} for CGB2 shows special transitional variations where a secondary increase in a_c^{BV} is observed after about ε_a>28%. Referring to Eq. 7, a_c is a scalar parameter where a_c=0 means fabric anisotropy. In this sense, a_c does not convey spatial information regarding whether the soil fabric vectors are more oriented in the vertical direction or horizontal direction. For instance, particle orientation is more significant in the horizontal direction as the non-spherical particles align their longer axis in the horizontal plane during triaxial compression. The later increasing part of transitional point for a_c^{BV} of CGB2 reveals that the branch vector starts to become more significant in the horizontal plane.

The values of Φ^{CN}, Φ^{PO} and Φ^{BV} at ε_a=40% are termed as critical fabric anisotropy (Φ_{cri}^{CN}, Φ_{cri}^{PO} and Φ_{cri}^{BV}), and whose variations are correlated with OR in Fig. 16. As SGB has completely symmetric shape, so Φ^{CN} and Φ^{BV} are collinear, whereas Φ^{PO} can always be treated as isotropic. The evolution of Φ_{cri}^{CN} shows a scattering feature, being not clearly related to OR. Particularly, the significantly high value of Φ^{CN} for AGB2 is due to the identification of asperity-to-asperity contacts

for the CN estimation, where multiple asperity-to-asperity contacts were counted for two contacting non-spherical clumps due to its planar shape when their bodies are contacting other than their tips. Nie *et al*., (2021) reported that the fabric anisotropy in terms of CN is more significant for more irregular materials, in which a more systematic alteration of particle morphology was considered. By contrast, more irregular materials exhibit more pronounced Φ_{cri}^{PO} during loading, being more significant in the directions perpendicular to the loading direction. Φ_{cri}^{BV} also displays an increasing trend with OR with a similar slope of that Φ_{cri}^{PO} against OR, while crossing the fabric isotropic line. This means that Φ_{cri}^{BV} can be either more significant in the vertical or horizontal direction. More irregular materials tend to distribute more BV in the horizontal directions while more sphere-like materials show an opposite effect.

Linking experimental and numerical observations of $\left(q/p'\right)_{cri}$ *with soil fabric*

Fig. 17 compares the critical stress ratios $\left(q/p'\right)_{cri}$ of simulation results obtained from this contribution to experimental results originally from Li *et al*. (2024) extrapolated to $\left(q/p'\right)_{cri}$ following Yilmaz *et al*. (2023). The simulation and experimental results are qualitatively comparable to reveal that more irregular particles lead to a higher stress level in the critical state. The reasons for the quantitative differences in this comparison are: 1) The samples had different shapes for each individual particle, leading to distributions of shape parameters like PSD (Li *et al*., 2024); whereas the DEM simulation considered the mono-dispersed shape distribution in each DEM sample. To highlight this, Fig. 17 provides horizontal bars to represent ±1 standard deviation of the particle shape distribution as outlined in Li *et al*. (2024). 2) Boundary conditions were different, with periodic boundaries in this contribution while lateral membrane conditions with rigid top and bottom walls in the laboratory (Li *et al*., 2021).

A shape-weighted fabric anisotropy index ($OR\Phi_{cri}^{PO}$ or $OR\Phi_{cri}^{BV}$) is newly proposed by combining OR with fabric anisotropy in the critical state. Fig. 18 shows that $(q/p')_{cri}$ is correlated well by the proposed index, indicating an essential role of shape-incorporated soil fabric in the stress response. Fig. 16 demonstrate that micro-structure of soils in the critical state is significantly affected by particle shape. Meanwhile, Li *et al.* (2021) revealed that elastic wave velocities in the critical state are influenced by the critical soil fabric at least for spherical particles. Wen and Zhang (2022) discovered the existence of a fabric surface in the critical state regardless of the shearing mode, where $(q/p')_{cri}$ is linearly correlated with strong-contact soil fabric. It can be concluded that the macroscopic response of soils is internally governed by microscopic parameters which are influenced by particle shape in the critical state. Therefore, incorporating the evolution of particle shape is a necessity when establishing constitutive models (*e.g.* Nguyen *et al*., 2020). In practice, since it is trivial to determine $(q/p')_{cri}$ physically and numerically, Fig. 18 builds the bridge towards predicting the microscopic critical soil fabric based on the macroscopic stress ratio in the critical state.

6. Conclusions

This contribution has systematically investigated the micro-to-macro response of granular materials with different particle shapes under the densest possible packings and monotonically sheared to the critical state in DEM virtual environment. Based on the simulation results, the following conclusions can be drawn:

- μCT is a powerful tool to reconstruct non-spherical particles for use in DEM simulations. With the given imaging data obtained from the granular materials tested in Li *et al*. (2024), N_s =25 is found to be a sufficient number to preserve 93% fidelity of S, C_x and OR, whereas a greater number of N_s is required to obtain AR closer to that of the originally irregular particle.

- Particle shape has a profound effect on the mechanical response of granular materials from small to large strains. As the particle becomes more irregular, q_{peak} and q_{cri}, e_{iso} and e_{cri}, $\overline{Z_{iso}}$ and $\overline{Z_{cri}}$ exhibit increasing trends.

- Small strain constants a decreases with increasing values of the monitored shape parameters; however, b seems to be less affected by particle shape but is influenced more by surface topography. M, λ and e^{Γ} are affected by particle shape and give lower values with the increase of shape parameters; $\overline{Z}^{\Gamma}$ and $\lambda_{\overline{Z}}$ are also found to be shape sensitive, with a decreasing tendency as shape parameters increase.

- The evolution of soil fabric demonstrates different behaviours for different particle shapes during shearing. CN progressively becomes more significant in the loading direction while PO shows the opposite trend during loading. By contrast, BV initially increases while stabilising or decreasing with further shearing, influenced by particle shape. In the critical state, samples with more sphere-like particles present less significant fabric anisotropy in terms of PO, BV demonstrates a transition from more vertically to more horizontally significant fabric response as particles become more irregular.

- $\left(q/p'\right)_{cri}$ from DEM simulations captures the laboratory results that used the granular materials for the non-spherical clump generation. Furthermore, the shape-weighted fabric indices ($OR\Phi_{cri}^{PO}$ or $OR\Phi_{cri}^{BV}$) are newly introduced to linearly capture the $\left(q/p'\right)_{cri}$ values, which is expected to predict microscopic soil fabric in the critical state using macroscopic stresses.

This contribution aimed to explore the role of particle shape on the micro-to-macro characteristics of granular soils, with a particular focus on a more realistic reflection of their responses. For this, μCT was utilised to acquire high-resolution imaging data which ensures accurate three-dimensional shape characterisation and construction of non-spherical particles while preserving their morphological fidelity. A vastly wide selection of particle shapes used in laboratory experimentation was considered for a more general representation of granular materials in real-world conditions. Additionally, the simplified HM contact model which more accurately captured the non-linear contact

characteristics was applied considering the local asperities of the multi-sphere clumps. Several future directions are envisioned. First, there is a need to develop a constitutive framework that implicitly incorporates particle shape terms (*e.g.*, Vu *et al*., 2004). This contribution empirically proposed a correlation between $(q/p')_{cri}$ and the shape-weighted fabric indices, this can be further refined by introducing a shape variable that governs the critical state parameters into the constitutive law. Second, analytical studies (*e.g.* Rothenburg and Bathurst, 1989; Seyedi Hosseininia, 2013) have proposed the intrinsic relation between macroscopic deviatoric stress and microscopic shear-induced fabric anisotropy using idealized particle shapes. It would be interesting to numerically validate their theoretical relations using more complex particle morphology adopted in this contribution. Another promising direction involves exploring the combined effect of particle shape and surface roughness. Natural occurring soils have multiscale particle morphology (Barrett, 1980), while this contribution has focused on the coarsest scale particle shape. Future work could use μCT and spherical harmonics (SH) to broadly assess particle morphology from particle shape to surface roughness (*e.g.*, Zhou *et al.*, 2015).

Acknowledgment

The contribution was funded by the Japan Society for the Promotion of Science (22K14322 and JPJSBP120195701), the UK Royal Society (IEC\R3\183026) and partially the UK Engineering and Physical Sciences Research Council (EPSRC) grant number EP/V053655/1. DEM simulations were performed using the Fujitsu PRIMERGY CX400M1/CX2550M5 (Oakbridge-CX) in the Information Technology Centre, the University of Tokyo.

Appendix

This appendix provides the formulae for calculating the shape parameters (S, C_x, AR and OR) especially used in this contribution based on Fig. A1.

$$S = \frac{\sqrt[3]{36\pi V_A^2}}{A} \tag{A1}$$

$$C_x = \frac{V_A}{V_C} \tag{A2}$$

$$AR = \frac{S_l}{L_l} \tag{A3}$$

$$OR = \left(S + C_x + AR\right)/3 \tag{A4}$$

where V_A and V_C are the volumes of a particle and its convex hull, respectively. A is the surface area of the particle. S_l, I_l, and L_l are the short, intermediate and long axes of the particle, respectively. For a three-dimensional object, flatness (S_l / I_l) and elongation (I_l / L_l) can describe a particle form in more spatial aspects, here the AR is considered as $S_l / L_l = \left(S_l / I_l\right) \cdot \left(I_l / L_l\right)$.

Notation

a, b	material-dependent constants to determine G_0
a_c	anisotropy degree
AR	aspect ratio
BV	branch vector
CN	contact normal
C_x	convexity
e	void ratio
e_{iso}, e_{cri}	e in the isotropic state and critical state
G_0	small strain shear stiffness
M, e^{Γ}, λ	critical state parameters
N_s	the number of sub-spheres to form one single clump
OR	overall regularity=($S + C_x + AR$)/3
p’	mean effective stress=($\sigma_1^{'}$+2$\sigma_3^{'}$)/3
PO	particle orientation
q	deviator stress = $\sigma_1^{'}$ - $\sigma_3^{'}$

q_{peak} , q_{cri} q in the peak state and critical state

q / p' deviator stress ratio

S sphericity

$\bar{Z}$ mean coordination number

$\overline{Z_{iso}}$, $\overline{Z_{cri}}$ $\bar{Z}$ in the isotropic state and critical state

$\bar{Z}^{\Gamma}$, $\lambda_{\bar{Z}}$ proposed critical state parameters for $\bar{Z}$

$\sigma_1^{'}$, $\sigma_3^{'}$ major and minor principal stresses ($\sigma_3^{'} = 50$ kPa)

μCT X-ray micro computed tomography

Φ_{11}, Φ_{22} , Φ_{33} second order fabric tensor in the three principal directions

Φ fabric ratio= $\Phi_{11} / [(\Phi_{22} + \Phi_{33})/2]$

ψ inclination of the soil fabric vectors relative to the horizontal plane

ε_a axial strain

ε_v volumetric strain

μ_{iso}, μ_{shear} interparticle friction coefficient during isotropic compression (=0.001) and triaxial compression (=0.35)

ζ_{local} , ζ_{vis} local and viscous damping coefficients

References

Altuhafi, F., O'Sullivan, C., Cavarretta, I. (2013) Analysis of an Image-Based Method to Quantify the Size and Shape of Sand Particles. Journal of Geotechnical and Geoenvironmental Engineering 139:1290-1307. doi.org/10.1061/(ASCE)GT.1943-5606.0000855

Altuhafi, F., Coop, M., Georgiannou, V. (2016) Effect of particle shape on the mechanical behavior of natural sands. Journal of Geotechnical and Geoenvironmental Engineering, 142(12), 04016071. doi.org/10.1061/(ASCE)GT.1943-5606.0001569

Angelidakis, V., Nadimi, S., Otsubo, M., Utili, S. (2021a) CLUMP: A Code Library to generate Universal Multi-sphere Particles. SoftwareX 15:100735. doi.org/10.1016/j.softx.2021.100735

Angelidakis, V., Nadimi, S., Utili, S. (2021b) SHape Analyser for Particle Engineering (SHAPE): Seamless characterisation and simplification of particle morphology from imaging data. Computer Physics Communications 265:107983. doi.org/10.1016/j.cpc.2021.107983

Angelidakis, V., Nadimi, S., Utili, S. (2022). Elongation, flatness and compactness indices to characterise particle form. Powder Technology, 396, 689-695. doi: 10.1016/j.powtec.2021.11.027

Barrett, P. (1980) The shape of rock particles, a critical review. Sedimentology 27:291-303. doi.org/10.1111/j.1365-3091.1980.tb01179.x

Chang, C.S., Misra, A., Sundaram, S.S. (1991). Properties of granular packings under low amplitude cyclic loading. Soil Dynam. Earthquake Engng 10, No. 4, 201–211. doi.org/10.1016/0267-7261(91)90034-W

Cho, G., Dodds, J., Santamarina, J. (2006) Particle Shape Effects on Packing Density, Stiffness, and Strength: Natural and Crushed Sands. Journal of Geotechnical and Geoenvironmental Engineering 132:591-602. doi.org/10.1061/(ASCE)1090-0241(2006)132:5(591)

Favier, J., Abbaspour-Fard, M., Kremmer, M., Raji, A. (1999) Shape representation of axi-symmetrical, non-spherical particles in discrete element simulation using multi-element model particles. Engineering Computations 16:467-480. doi.org/10.1108/02644409910271894

Fonseca, J., O'Sullivan, C., Coop, M. R., Lee, P. D. (2013). Quantifying the evolution of soil fabric during shearing using directional parameters. Géotechnique, 63(6), 487–499. doi.org/10.1680/geot.12.p.003

Hardin, B., Richart, F. (1963) Elastic Wave Velocities in Granular Soils. Journal of the Soil Mechanics and Foundations Division 89:33-65. doi.org/10.1061/JSFEAQ.0000493

Itasca Consulting Group (2007) PFC3D version 4.0 user manual Minneapolis.

Iwasaki, T., Tatsuoka, F. (1977). Effects of grain size and grading on dynamic shear moduli of Sands. Soils and Foundations, 17(3), 19–35. doi.org/10.3208/sandf1972.17.3_19

Jiang, M. D., Yang, Z. X., Barreto, D., Xie, Y. H. (2018). The influence of particle-size distribution on critical state behavior of spherical and non-spherical particle assemblies. Granular Matter, 20(4). doi.org/10.1007/s10035-018-0850-x

Johnson, K.L. (1985). Contact mechanics, Cambridge, UK: Cambridge University Press.

Katagiri, J. (2019) A novel way to determine number of spheres in clump-type particle-shape approximation in discrete-element modelling. Géotechnique 69:620-626. doi.org/10.1680/jgeot.18.P.021

Katagiri, J., Matsushima, T., Yamada, Y. (2010). Simple shear simulation of 3D irregularly-shaped particles by image-based dem. Granular Matter, 12(5), 491–497. doi.org/10.1007/s10035-010-0207-6

Kawamoto, R., Andò, E., Viggiani, G., Andrade, J. E. (2016). Level set discrete element method for three-dimensional computations with triaxial case study. Journal of the Mechanics and Physics of Solids, 91, 1–13. doi.org/10.1016/j.jmps.2016.02.021

Kawamoto, R., Andò, E., Viggiani, G., Andrade, J. E. (2018). All you need is shape: Predicting shear banding in sand with LS-DEM. Journal of the Mechanics and Physics of Solids, 111, 375–392. doi.org/10.1016/j.jmps.2017.10.003

Krumbein, W. C., Sloss, L. L. (1963) Stratigraphy and sedimentation, 2nd Ed., Freeman, San Francisco.

Kuwano, R., Jardine, R. J. (2002). On the applicability of cross-anisotropic elasticity to granular materials at very small strains. Géotechnique, 52(10), 727–749. doi.org/10.1680/geot.2002.52.10.727

Li, Y., Otsubo, M., Kuwano, R. (2021). DEM analysis on the stress wave response of spherical particle assemblies under triaxial compression. Computers and Geotechnics, 133, 104043. doi.org/10.1016/j.compgeo.2021.104043

Li, Y., Otsubo, M., Liu, J., & Kuwano, R. (2024). Effect of particle morphology on stress and strain characteristics of granular materials during triaxial compression. Acta Geotechnica, doi.org/10.1007/s11440-023-02190-y

Li, Y., Otsubo, M., Kuwano, R. (2022a). Interpretation of static and dynamic young's moduli and Poisson's ratio of granular assemblies under shearing. Computers and Geotechnics, 142, 104560. doi.org/10.1016/j.compgeo.2021.104560

Li, Y., Otsubo, M., Ghaemi, A., Dutta, T. T., Kuwano, R. (2022b). Transition of gap-graded soil fabric – shear wave measurements and dispersion relation. Soils and Foundations, 62(1), 101092. doi.org/10.1016/j.sandf.2021.101092

Liu, X., Yang, J. (2018). Shear wave velocity in sand: Effect of grain shape. Géotechnique, 68(8), 742–748. doi.org/10.1680/jgeot.17.t.011

Lopera Perez, J., Kwok, C., O′Sullivan, C., Huang, X., Hanley, K. (2016) Assessing the quasi-static conditions for shearing in granular media within the critical state soil mechanics framework. Soils and Foundations, 56(1), pp.152-159. doi.org/10.1016/j.sandf.2016.01.013

Morimoto, T., Otsubo, M., Koseki, J. (2021) Microscopic investigation into liquefaction resistance of pre-sheared sand: Effects of particle shape and initial anisotropy. Soils and Foundations 61:335-351. doi.org/10.1016/j.sandf.2020.12.008

Nadimi, S., Fonseca, J., (2018) A micro finite-element model for soil behaviour. Géotechnique, 68(4), pp.290-302. doi.org/10.1680/jgeot.16.P.147

Nguyen, T. D., Plimpton, S. J. (2019). Aspherical particle models for molecular dynamics simulation. Computer Physics Communications, 243, 12–24. doi.org/10.1016/j.cpc.2019.05.010

Nguyen, H. B., Rahman, M. M., Fourie, A. B. (2020). Effect of particle shape on constitutive relation: DEM Study. Journal of Geotechnical and Geoenvironmental Engineering, 146(7). doi.org/10.1061/(asce)gt.1943-5606.0002278

Nguyen, H., Rahman, M., Fourie, A. (2021) How particle shape affects the critical state, triggering of instability and dilatancy of granular materials – results from a DEM study. Géotechnique 71:749-764. doi.org/10.1680/jgeot.18.P.211

Nie, J. Y., Zhao, J., Cui, Y. F., Li, D. Q. (2021). Correlation between grain shape and critical state characteristics of uniformly graded sands: A 3D DEM study. Acta Geotechnica, 17(7), 2783–2798. doi.org/10.1007/s11440-021-01362-y

Nie, J., Shi, X., Cui, Y., Yang, Z. (2022). Numerical evaluation of particle shape effect on small strain properties of granular soils. Engineering Geology, 303, 106652. doi.org/10.1016/j.enggeo.2022.106652

Oda, M. (1982). Fabric tensor for discontinuous geological materials. Soils and Foundations, 22(4), 96–108. doi.org/10.3208/sandf1972.22.4_96

O'Sullivan, C., Bray, J. (2004) Selecting a suitable time step for discrete element simulations that use the central difference time integration scheme. Engineering Computations 21:278-303.doi.org/10.1108/02644400410519794

Otsu, N. (1979) A threshold selection method from gray-level histograms. IEEE Trans. Systems, Man and Cybernetics 9, No. 1, 62–66. doi: 10.1109/TSMC.1979.4310076

Otsubo, M., O'Sullivan, C., Shire, T. (2017). Empirical assessment of the critical time increment in explicit particulate discrete element method simulations. Computers and Geotechnics, 86, 67–79. doi.org/10.1016/j.compgeo.2016.12.022

Otsubo, M., O'Sullivan, C. (2018). Experimental and DEM assessment of the stress-dependency of surface roughness effects on shear modulus. Soils and Foundations, 58(3), 602–614. doi.org/10.1016/j.sandf.2018.02.020

Otsubo, M., Li, Y., Kuwano, R., Nadimi, S., Vasileios, A. (2023) Contact-scale insights into G_0 development of non-spherical particle assembly. Géotechnique, under review.

Plimpton, S. (1995) Fast Parallel Algorithms for Short-Range Molecular Dynamics. Journal of Computational Physics 117:1-19. doi.org/10.1006/jcph.1995.1039

Rothenburg, L., Bathurst, R. J. (1989). Analytical study of induced anisotropy in idealized granular materials. Géotechnique, 39(4), 601–614. https://doi.org/10.1680/geot.1989.39.4.601

Salot, C., Gotteland, P., Villard, P. (2009). Influence of relative density on granular materials behavior: DEM simulations of triaxial tests. Granular Matter, 11(4), 221–236. doi.org/10.1007/s10035-009-0138-2

Seyedi Hosseininia, E. (2013). Stress–force–fabric relationship for planar granular materials. Géotechnique, 63(10), 830–841. https://doi.org/10.1680/geot.12.p.055

Shin, H., Santamarina, J. (2013) Role of Particle Angularity on the Mechanical Behavior of Granular Mixtures. Journal of Geotechnical and Geoenvironmental Engineering 139:353-355. doi.org/10.1061/(ASCE)GT.1943-5606.0000768

Thornton, C. (2000) Numerical simulations of deviatoric shear deformation of granular media. Géotechnique 50, No. 1, 43-53. doi.org/10.1680/geot.2000.50.1.43

Vu, D. C., Amarsid, L., Delenne, J.-Y., Richefeu, V., Radjai, F. (2023). Macro-elasticity of granular materials composed of polyhedral particles. Granular Matter, 26(1). doi.org/10.1007/s10035-023-01382-3

Wen, Y., Zhang, Y. (2022). Evidence of a unique critical fabric surface for granular soils. Géotechnique, 1–16. doi.org/10.1680/jgeot.21.00126

Wichtmann, T., Triantafyllidis, T. (2009). Influence of the grain-size distribution curve of quartz sand on the small strain shear modulus gmax. Journal of Geotechnical and Geoenvironmental Engineering, 135(10), 1404–1418. doi.org/10.1061/(asce)gt.1943-5606.0000096

Wu, Y., Cui, J., Huang, J., Zhang, W., Yoshimoto, N., Wen, L. (2021). Correlation of critical state strength properties with particle shape and surface fractal dimension of clinker ash. International Journal of Geomechanics, 21(6). doi.org/10.1061/(asce)gm.1943-5622.0002027

Xiao, Y., Long, L., Matthew Evans, T., Zhou, H., Liu, H., Stuedlein, A., (2019) Effect of Particle Shape on Stress-Dilatancy Responses of Medium-Dense Sands. Journal of Geotechnical and Geoenvironmental Engineering 145:04018105. doi.org/10.1061/(ASCE)GT.1943-5606.0001994

Xie, Y. H., Yang, Z. X., Barreto, D., Jiang, M. D. (2017). The influence of particle geometry and the intermediate stress ratio on the shear behavior of granular materials. Granular Matter, 19(2). doi.org/10.1007/s10035-017-0723-8

Xu, M., Guo, N., Yang, Z. (2021). Particle shape effects on the shear behaviors of granular assemblies: irregularity and elongation. Granular Matter, 23(2). doi: 10.1007/s10035-021-01096-4

Yang, J., Luo, X. (2015) Exploring the relationship between critical state and particle shape for granular materials. Journal of the Mechanics and Physics of Solids 84:196-213. doi.org/10.1016/j.jmps.2015.08.001

Yilmaz, Y., Deng, Y., Chang, C. S., Gokce, A. (2023). Strength–dilatancy and critical state behaviours of binary mixtures of graded sands influenced by particle size ratio and fines content. Géotechnique, 73(3), 202–217. doi.org/10.1680/jgeot.20.p.320

Zhang, N., Hedayat, A., Han, S., Yang, R., Bolaños Sosa, H., González Cárdenas, J., Salas Álvarez, G. (2021) Isotropic compression behavior of granular assembly with non-spherical particles by X-ray micro-computed tomography and discrete element modeling. Journal Of Rock Mechanics and Geotechnical Engineering, 13(5), 972-984. doi: 10.1016/j.jrmge.2021.04.005

Zhao, J., Zhao, S., Luding, S. (2023). The role of particle shape in computational modelling of Granular Matter. Nature Reviews Physics. doi.org/10.1038/s42254-023-00617-9

Zhao, S., Zhou, X. (2017). Effects of particle asphericity on the macro- and micro-mechanical behaviors of granular assemblies. Granular Matter, 19(2). doi.org/10.1007/s10035-017-0725-6

Zhao, S., Zhang, N., Zhou, X., Zhang, L. (2017) Particle shape effects on fabric of granular random packing. Powder Technology 310:175-186. doi.org/10.1016/j.powtec.2016.12.094

Zheng, J., Hryciw, R. D. (2017). Soil particle size and shape distributions by stereophotography and image analysis. Geotechnical Testing Journal, 40(2), 20160165. doi.org/10.1520/gtj20160165

Zhou, B., Wang, J., Zhao, B. (2015). Micromorphology characterization and reconstruction of sand particles using micro x-ray tomography and spherical harmonics. Engineering Geology, 184, 126–137. doi.org/10.1016/j.enggeo.2014.11.009

Accepted manuscript doi:
10.1680/jgeot.23.00162

Table 1 Shape parameters of μCT imaging data and non-spherical clumps (N_s =25) of tested materials.

ID	Sphericity: S			Convexity: C_x			Aspect ratio: AR			Overall regularity: OR		
	DEM	μCT	Diff [%]	DEM	μCT	Diff [%]	DEM	μCT	Diff [%]	DEM	μCT	Diff [%]
SGB	1.000	0.940	6.4	1.000	0.974	2.7	1.000	0.975	2.6	1.000	0.963	3.8
DGB	0.890	0.916	-2.8	1.000	0.936	6.8	0.900	0.918	-1.9	0.930	0.923	0.7
CGB1	0.862	0.888	-3.0	0.907	0.901	0.6	0.746	0.766	-2.6	0.838	0.852	-1.6
CGB2	0.651	0.671	-3.0	0.541	0.568	-4.8	0.508	0.443	14.7	0.567	0.561	1.1
AGB1	0.715	0.715	-0.04	0.807	0.807	0.04	0.405	0.405	-0.1	0.642	0.642	-0.02
AGB2	0.537	0.537	0.02	0.739	0.739	0.06	0.231	0.281	-17.9	0.502	0.519	-3.2
LBS	0.799	0.799	-0.1	0.847	0.847	0.02	0.882	0.882	0.0	0.843	0.843	-0.01
SS	0.825	0.860	-4.1	0.857	0.886	-3.2	0.877	0.802	9.4	0.853	0.849	0.4

Table 2 Mechanical response quantities, small strain material constants and critical state parameters of tested materials.

ID	e_{iso}	e_{cri}	$\overline{Z_{iso}}$	$\overline{Z_{cri}}$	q_{peak} [kPa]	q_{cri} [kPa]	$\varepsilon_{v,cri}$ [%]	a [MPa]	b	M	λ	e^{Γ}	$\lambda_{\bar{Z}}$	$\bar{Z}^{\Gamma}$
SGB	0.529	0.656	5.68	4.05	78.2	49.5	-8.32	638.9	0.356	0.70	0.0026	0.440	0.064	3.81
DGB	0.448	0.623	9.80	4.42	136.4	55.2	-14.7	517.6	0.355	0.77	0.0019	0.660	0.140	3.80
CGB1	0.452	0.682	8.15	5.56	156.5	73.9	-15.7	871.0	0.353	0.97	0.0022	0.685	0.175	4.82
CGB2	0.803	1.282	11.98	7.15	248.9	130.1	-25.5	1868.8	0.349	1.19	0.0275	1.396	0.433	5.31
AGB1	0.589	0.902	12.17	7.15	176.3	104.9	-19.7	705.2	0.348	1.19	0.0128	0.962	0.565	5.56
AGB2	0.860	1.248	12.14	7.42	185.4	146.4	-20.7	1603.8	0.345	1.37	0.0427	1.448	0.763	6.70
LBS	0.516	0.803	12.14	6.79	176.8	80.1	-18.9	538.5	0.354	1.05	0.0065	0.831	0.464	4.72
SS	0.510	0.828	10.70	6.64	181.4	84.3	-20.7	536.2	0.356	1.05	0.0044	0.847	0.472	4.53

Accepted manuscript doi:
10.1680/jgeot.23.00162

Figure captions

Fig. 1 Schematic of image-processing and clump-generation operations. A grayscale μCT image is binarised, the different particles are segmented, labelled, and then approximated by multi-spheres.

Fig. 2 Evolution of shape parameters (S, C_x, AR and OR) for increasing the number of sub-spheres (N_s) with examples of non-spherical clumps generated from μCT imaging data of a silica sand particle.

Fig. 3 Generated particle shapes for a spherical glass bead (SGB, N_s=1) and for non-spherical particles (N_s=25) of deformed glass beads (DGB), clumped glass beads (CGB1, CGB2), angular glass beads (AGB1, AGB2), Leighton Buzzard sand (LBS) and silica sand (SS).

Fig. 4 Representative example of a cubical sample composed of non-spherical clumps originally from SS using N_s=25 sub-spheres per particle.

Fig. 5 Deviator stress (q) and volumetric strain (ε_v) against axial strain (ε_a) during triaxial compression for eight different particle shapes with isotropic stress of p'=50kPa: (a) q - ε_a (b) ε_v - ε_a. All samples were prepared under their densest packing configuration.

Fig. 6 Void ratio (e) and mean coordination number ($\bar{Z}$) against axial strain (ε_a) for eight different particle shapes during triaxial compression (a) e - ε_a (b) $\bar{Z}$ - ε_a. All samples were prepared under their densest packing configuration.

Fig. 7 Relations between (a) peak/critical deviator stress ratios $(q/p')_{peak}$ and $(q/p')_{cri}$ (b) isotropic/critical void ratios e_{iso} and e_{cri} (c) isotropic/critical mean coordination numbers $\overline{Z_{iso}}$ and $\overline{Z_{cri}}$ and shape parameters *S*, C_x, *AR* and *OR*.

Fig. 8 Relations between material constant (a) in Eq. 1 and shape parameters S, C_x, AR and OR.

Fig. 9 Relations between critical state parameter (M) in Eq. 2 and shape parameters S, C_x, AR and OR.

Fig. 10 Relations between critical state parameter (a) λ and (b) e^{Γ} for void ratio (e) in Eq. 3 and shape parameters S, C_x, AR and OR.

Fig. 11 Relations between critical state parameters (a) $\lambda_{\bar{Z}}$ and (b) $\bar{Z}^{\Gamma}$ for mean coordination number ($\bar{Z}$) in Eq. 4 and shape parameters S, C_x, AR and OR.

Fig. 12 Normalised frequency distributions of angles of contact normal (ψ^{CN}), particle orientation (ψ^{PO}) and branch vector (ψ^{BV}) relative to the horizontal direction for SS at selected axial strains (ε_a) during triaxial compression.

Fig. 13 Distributions of the three-dimensional orientations of normalised soil fabric indices for SS at selected axial strains (ε_a) during triaxial compression.

Accepted manuscript doi:
10.1680/jgeot.23.00162

Fig. 14 Variations of fabric anisotropy indices for contact normal (Φ^{CN}), particle orientation (Φ^{PO}) and branch vector (Φ^{BV}) of SS and CGB2 with axial strain (ε_a) during triaxial compression under their initial densest packing configuration.

Fig. 15 Variations of anisotropy degrees for contact normal (a_c^{CN}), particle orientation (a_c^{PO}) and branch vector (a_c^{BV}) of SS and CGB2 with axial strain (ε_a) during triaxial compression under their initial densest packing configuration.

Fig. 16 Correlations between overall regularity (OR) and fabric anisotropy indices in the critical state (contact normal (Φ_{cri}^{CN}), particle orientation (Φ_{cri}^{PO}) and branch vector (Φ_{cri}^{BV})).

Fig. 17 Comparison of critical deviator stress ratios $(q/p')_{cri}$ against overall regularity (OR) between DEM simulation results (this contribution) and laboratory data (from Li *et al*. (2024)), where real particles were used to generate non-spherical clumps in this contribution.

Fig. 18 Correlation between critical deviator stress ratio $(q/p')_{cri}$ and shape-weighted fabric anisotropy indices ($OR\Phi_{cri}^{PO}$ or $OR\Phi_{cri}^{BV}$) in the critical state.

Fig. A1 Illustration of geometric particle parameters in three dimensions. The outer envelope curve shows the convex hull of the particle, while the noted parameters are the short, intermediate and long particle axes (S_l, I_l, L_l), the particle volume (V_A) and the volume of its convex hull (V_C).

Accepted manuscript doi:
10.1680/jgeot.23.00162

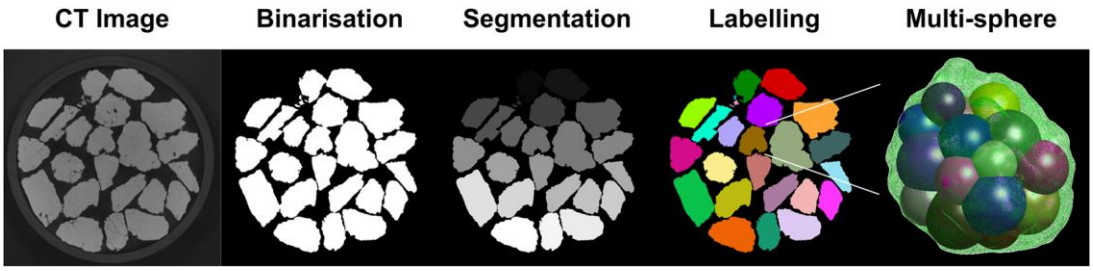

Fig.1

Accepted manuscript doi:
10.1680/jgeot.23.00162

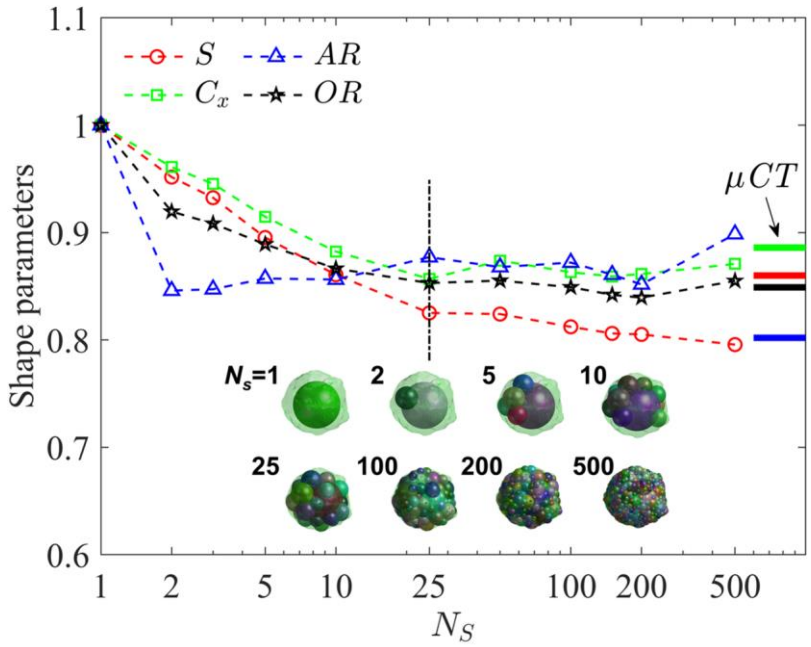

Fig.2

Accepted manuscript doi:
10.1680/jgeot.23.00162

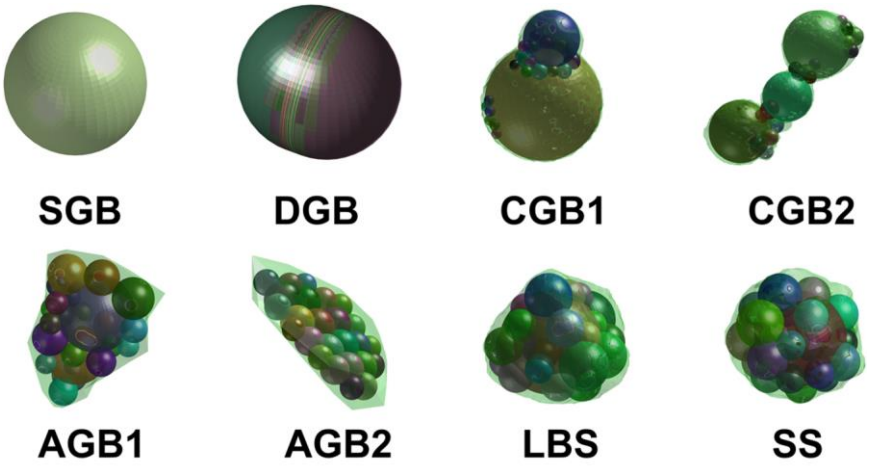

Fig.3

Accepted manuscript doi:
10.1680/jgeot.23.00162

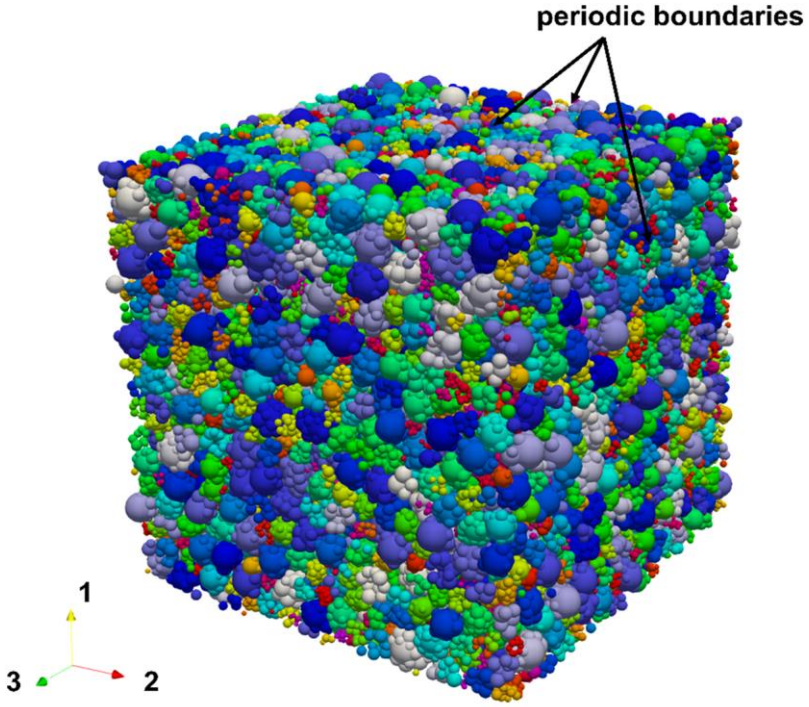

Fig.4

Accepted manuscript doi:
10.1680/jgeot.23.00162

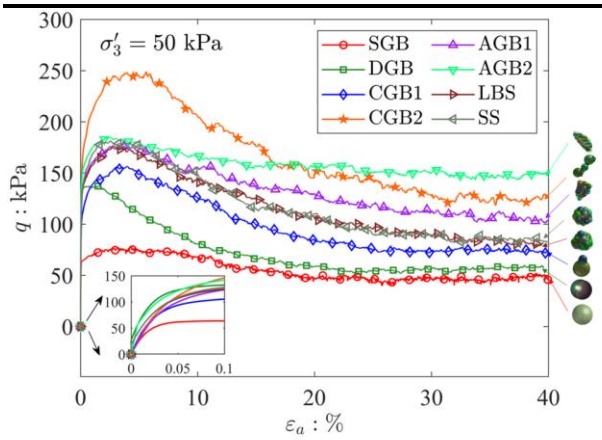

Fig.5a

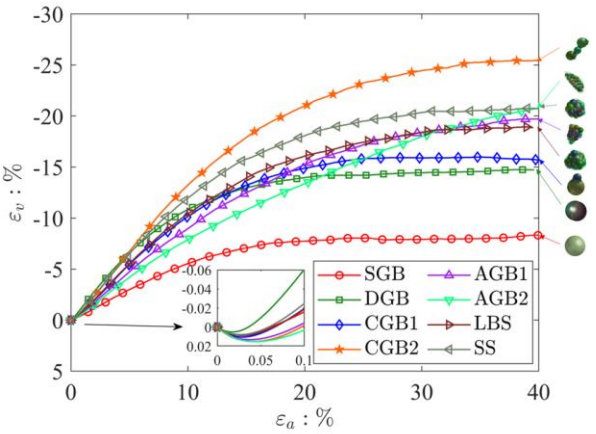

Fig.5b

Accepted manuscript doi:
10.1680/jgeot.23.00162

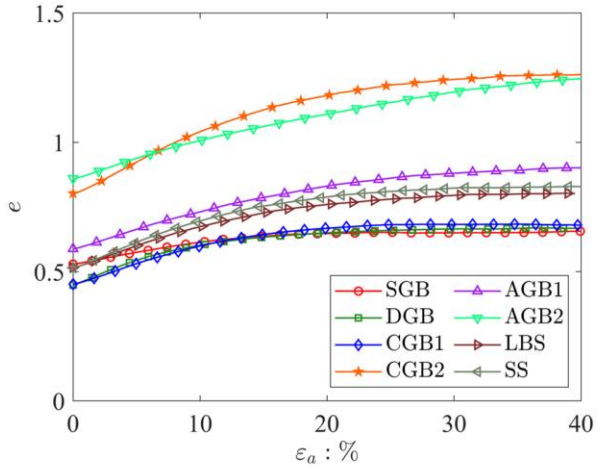

Fig.6a

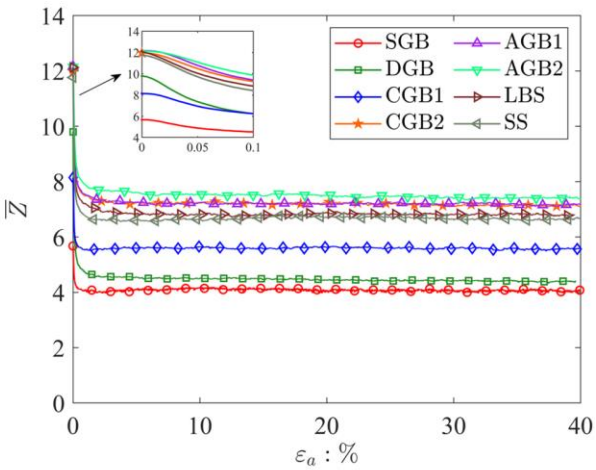

Fig.6b

Accepted manuscript doi:
10.1680/jgeot.23.00162

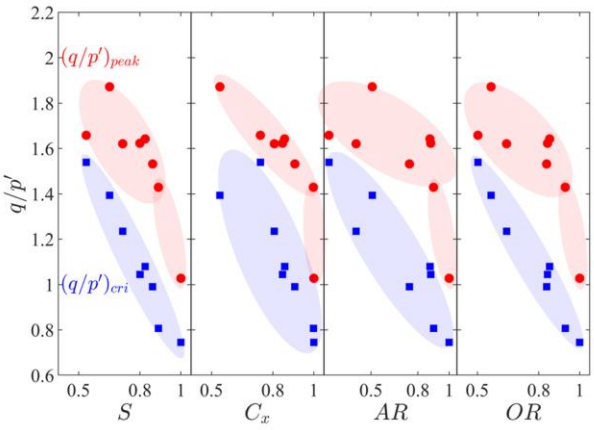

Fig.7a

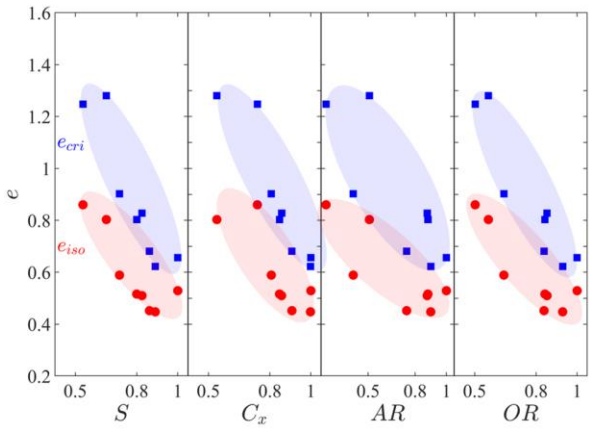

Fig.7b

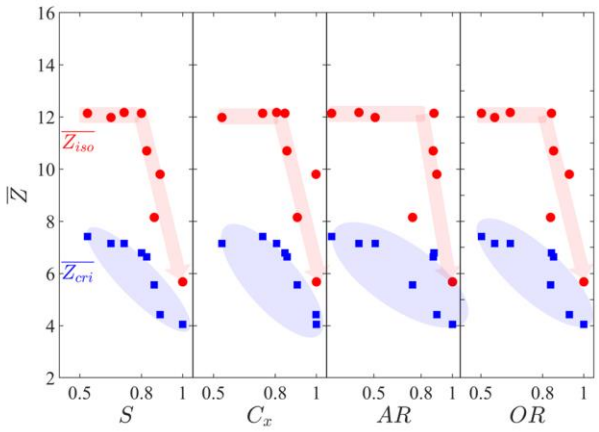

Fig.7c

Accepted manuscript doi:
10.1680/jgeot.23.00162

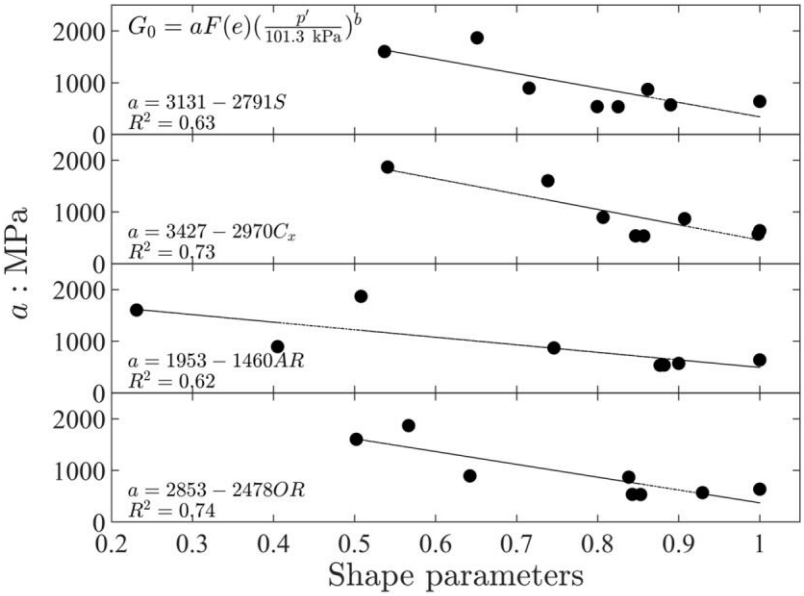

Fig.8

Accepted manuscript doi:
10.1680/jgeot.23.00162

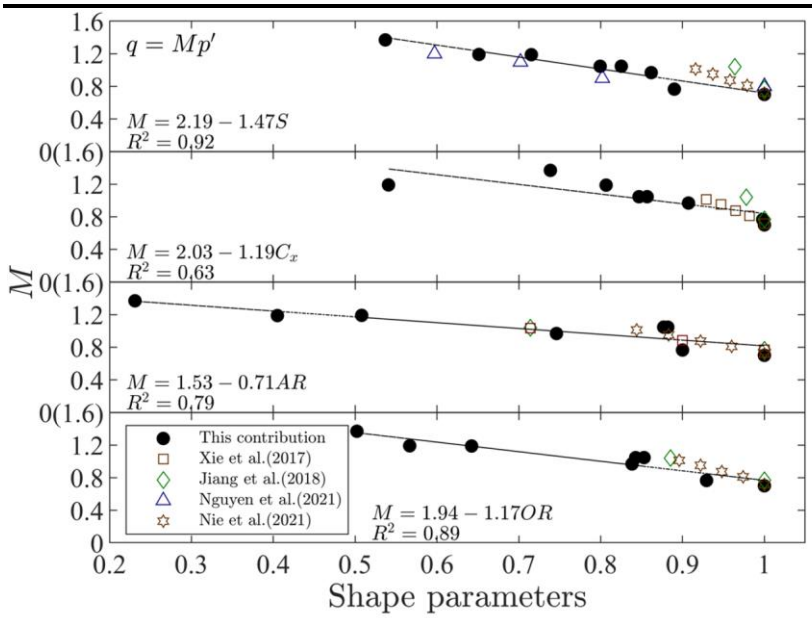

Fig.9

Accepted manuscript doi:
10.1680/jgeot.23.00162

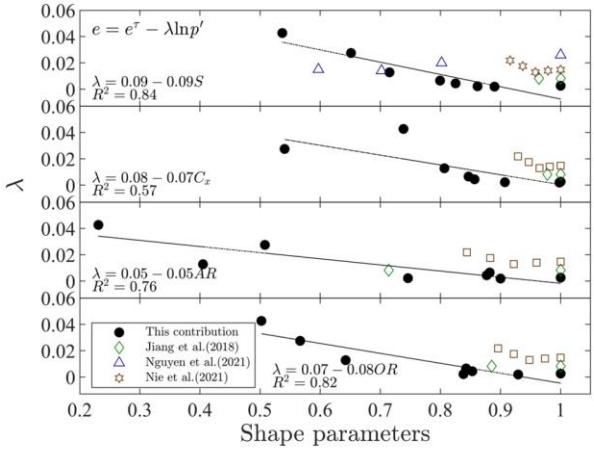

Fig.10a

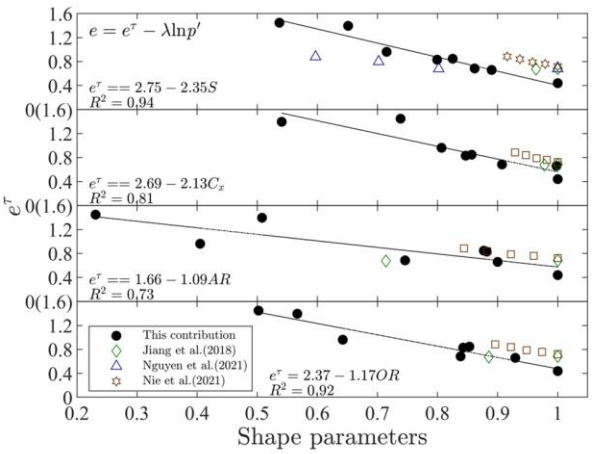

Fig.10b

Accepted manuscript doi:
10.1680/jgeot.23.00162

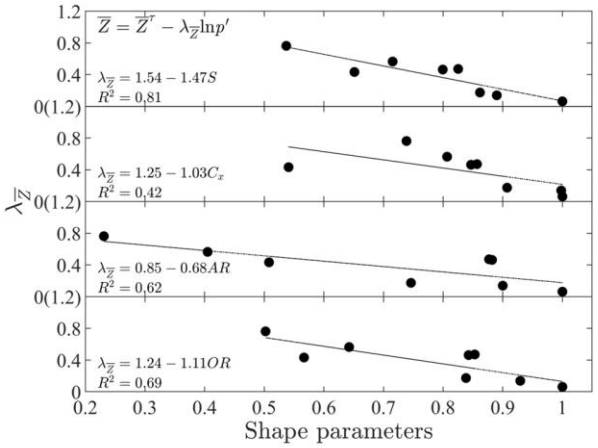

Fig.11a

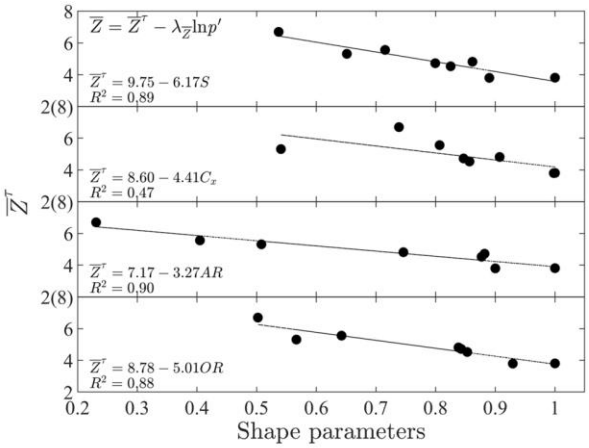

Fig.11b

Accepted manuscript doi:
10.1680/jgeot.23.00162

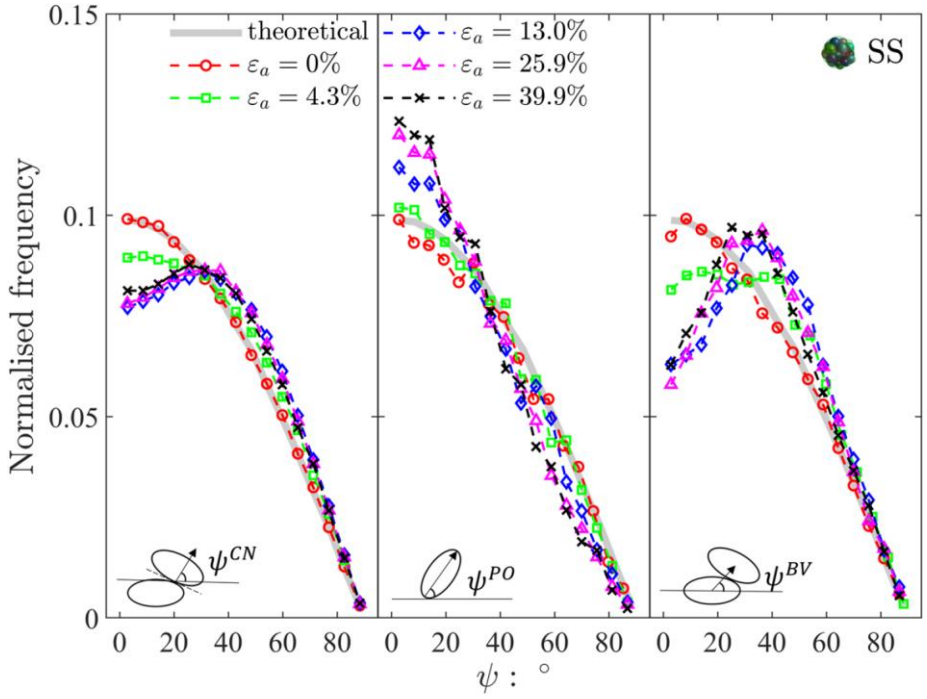

Fig.12

Accepted manuscript doi:
10.1680/jgeot.23.00162

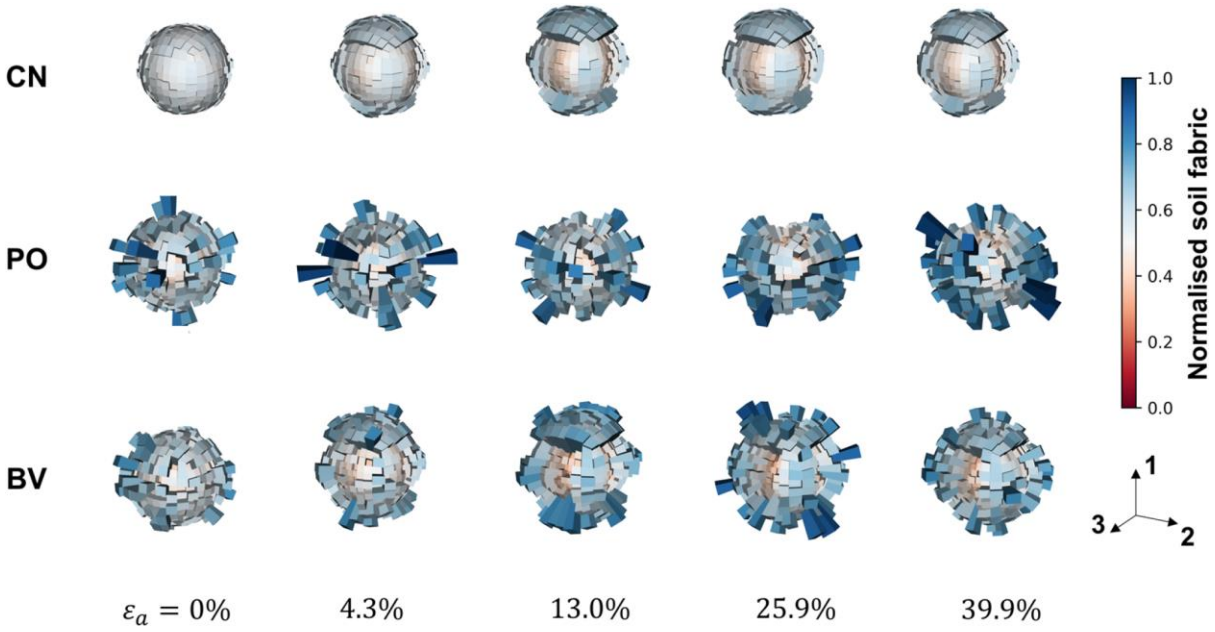

Fig.13

Accepted manuscript doi:
10.1680/jgeot.23.00162

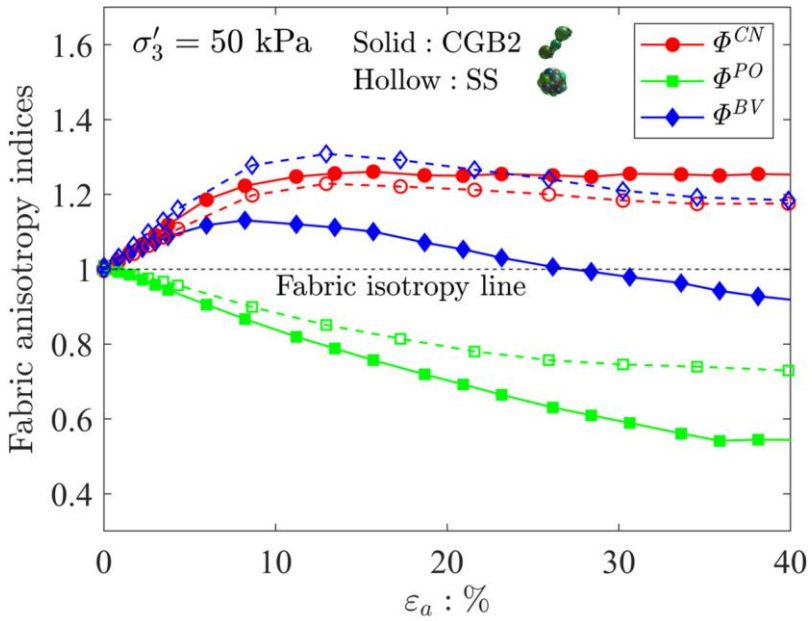

Fig.14

Accepted manuscript doi:
10.1680/jgeot.23.00162

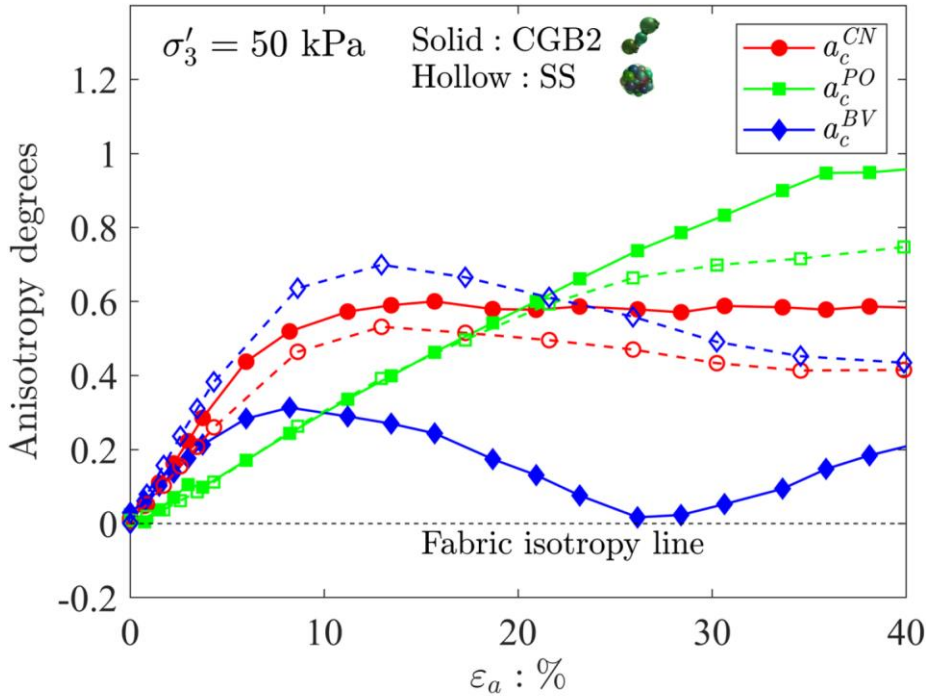

Fig.15

Accepted manuscript doi:
10.1680/jgeot.23.00162

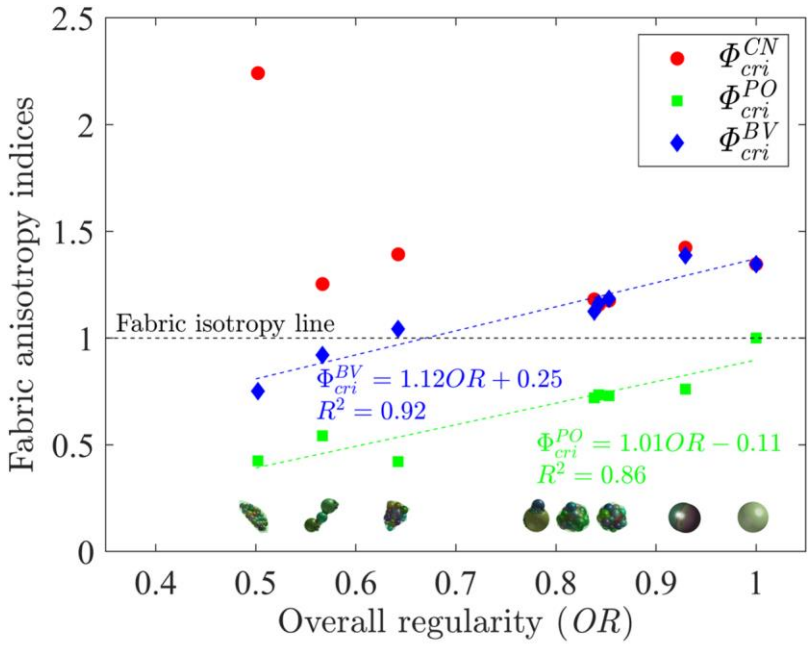

Fig.16

Accepted manuscript doi:
10.1680/jgeot.23.00162

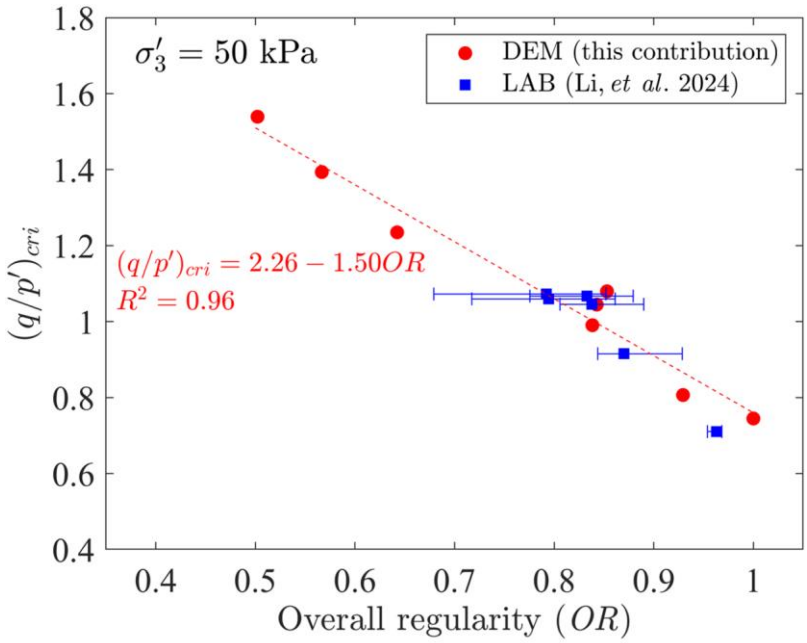

Fig.17

Accepted manuscript doi:
10.1680/jgeot.23.00162

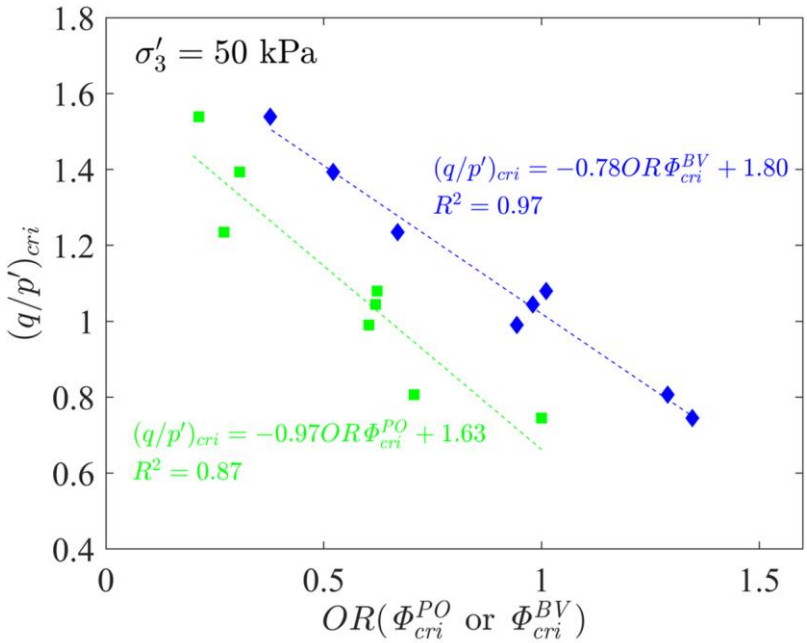

Fig.18

Accepted manuscript doi:
10.1680/jgeot.23.00162

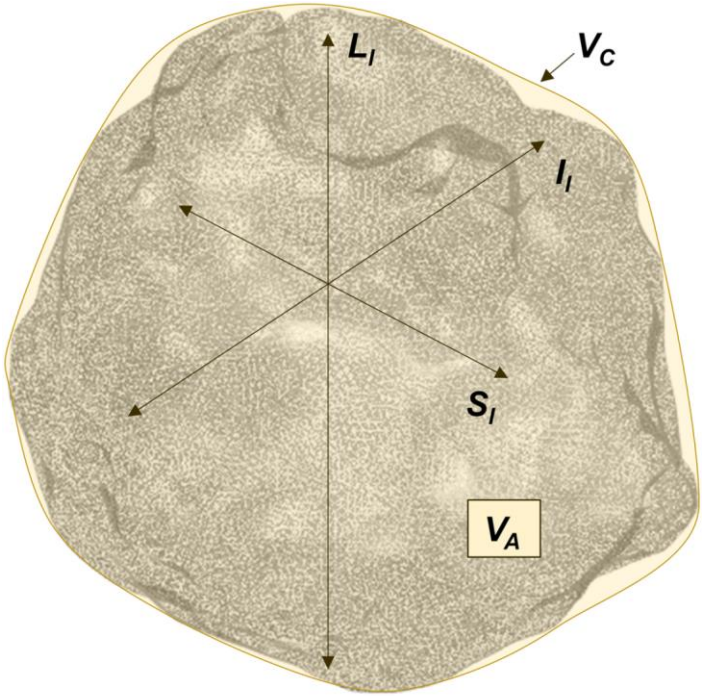

Fig.A1